VIRTUAL AND PHYSICAL PROTOTYPING
2025, VOL. 20, NO. 1, e2457580 (10 pages)
https://doi.org/10.1080/17452759.2025.2457580

Taylor & Francis
Taylor & Francis Group

Multi-material 3D printed smart floor tiles with triboelectric energy generation and security monitoring

Shidhin Mappoli[a], Kalyan Ghosh[a] and Martin Pumera[a,b,c,d,e]

[a]Future Energy and Innovation Laboratory, Central European Institute of Technology, Brno University of Technology (CEITEC-BUT), Brno, Czech Republic; [b]Energy Research Institute@NTU (ERI@N), Research Techno Plaza, Singapore, Singapore; [c]Advanced Nanorobots & Multiscale Robotics Laboratory, Faculty of Electrical Engineering and Computer Science, VSB – Technical University of Ostrava, Ostrava, Czech Republic; [d]Department of Medical Research, China Medical University Hospital, China Medical University, Taichung, Taiwan; [e]Department of Chemical and Biomolecular Engineering, Yonsei University, Seoul, Republic of Korea

ABSTRACT

With the growing demand for integrated smart home systems driven by advancements in the Internet of Things (IoT) and smart city initiatives, the need for efficient, simple, and self-sustaining sensors has become essential. Triboelectric nanogenerators (TENGs) have recently emerged as a promising device for both energy harvesting and sensing. However, the fabrication of different TENG layers using conventional techniques is often complex, time-intensive, and involves multiple processing steps. Here, a single-step multi-material 3D printing (MMP) approach is used to fabricate the fully functional TENG device, consisting of positive and negative triboelectric layers, current collectors and supporting substrate. Nylon 6 and carbon/polyvinylidene fluoride (C/PVDF) filaments are selected for positive and negative triboelectric layers, respectively and conductive carbon/polylactic acid (C/PLA) filament was selected for both current collectors and wood/PLA is selected for both top and bottom supporting layers. The MMP-TENG is integrated with electronics to showcase its capability for remote monitoring in smart home settings to detect real-time fall detection and security monitoring. This research will pave the way for fabricating a smart floor for security monitoring and energy generation in a smart building.

ARTICLE HISTORY
Received 21 June 2024
Accepted 18 January 2025

KEYWORDS
3D-printing; multi-material printing; TENG; smart floor; smart building

1. Introduction

In a world increasingly powered by data and automation, sensors have become a crucial component of modern devices, enabling real-time monitoring, efficient energy management, and seamless interactions within domestic environments [1–3]. Conventional sensing technologies, such as capacitive, resistive, piezoelectric, and optical sensors, are currently used to detect mechanical, electrical, or thermal changes [4–6]. Recently, triboelectric nanogenerators (TENGs) have emerged as self-powered sensors with dual functionality, serving both as energy harvesters and as capable devices for detecting various physical stimuli [7–12]. While the triboelectric effect has been known for centuries, the systematic generation of energy using this effect was only discovered in 2012 by Wang et al. with the development of the first TENG [13]. TENGs convert low-frequency mechanical energy to electrical energy by the principles of contact electrification and electrostatic induction. The triboelectric effect occurs when two different materials with different electron affinities come into contact and subsequently separate [14]. Usually, these materials are selected from triboelectric series, where the materials are arranged based on their tendency to gain or lose electrons [15, 16]. Commonly employed negative triboelectric or tribonegative materials include polydimethylsiloxane (PDMS), fluorinated ethylene propylene (FEP), polyvinylidene fluoride (PVDF), and polytetrafluoroethylene (PTFE), while materials such as human skin, hair, nylon 6, and cotton wool are frequently categorised as positive triboelectric or tribopositive materials. TENG output can be optimised and tuned by altering parameters such as contact-separation distance, frequency of contact,

CONTACT Martin Pumera martin.pumera@gmail.com Future Energy and Innovation Laboratory, Central European Institute of Technology, Brno University of Technology (CEITEC-BUT), Purkyňova 123, 61200 Brno, Czech Republic; Energy Research Institute@NTU (ERI@N), Research Techno Plaza, X-Frontier Block, Level 5, 50 Nanyang Drive, Singapore 637553, Singapore; Advanced Nanorobots & Multiscale Robotics Laboratory, Faculty of Electrical Engineering and Computer Science, VSB – Technical University of Ostrava, 17. listopadu 2172/15, Ostrava 70800, Czech Republic; Department of Medical Research, China Medical University Hospital, China Medical University, No 91 Hsueh-Shih Road, Taichung 40402, Taiwan; Department of Chemical and Biomolecular Engineering, Yonsei University, 50 Yonsei-ro, Seodaemun-gu, Seoul 03722, Republic of Korea

Supplemental data for this article can be accessed online at https://doi.org/10.1080/17452759.2025.2457580.

separation cycles, and contact area. Additionally, material properties such as electron affinity, surface work function, dielectric constant, and surface morphology play a major role in determining output efficiency [17–21].

Additive manufacturing, particularly 3D printing, has revolutionised device fabrication by allowing for rapid prototyping and customisable designs with minimal manufacturing processes. 3D-printed devices have demonstrated widespread applications ranging from wearable electronics to artificial prosthetics [22–24]. Among various 3D printing technologies, fused deposition modelling (FDM) is known for its fast and simple fabrication technologies with minimum operational requirements [25–27]. The recent addition of multi-material 3D printing (MMP) technology to FDM makes it more attractive due to the possibility of 3D printing entire devices in a single stretch [28, 29]. MMP technique improves design flexibility and material efficiency, which lowers wastage during manufacturing and facile incorporation of different materials in a single printed structure [29, 30]. These developments offer a significant edge over conventional device manufacturing practices that involve techniques such as lithography, etching, or moulding, which are complex, expensive and time-consuming. Lately, several articles have been published demonstrating the capabilities of MMP, which can be realised by different 3D printing techniques [28, 31, 32]. For example, 3D-printed multi-material grippers, [33] stretchable soft pressure sensors, [34] knee joint models, [35] etc. are fabricated using different MMP techniques such as FDM, extrusion-based direct-print system, and PolyJet 3D printing, respectively. However, challenges such as weak interlaminar adhesion between distinct polymeric materials can lead to delamination and compromised structural integrity [36]. To overcome this, strategies like surface roughness modification, mechanical interlocking, and optimised thermal management during printing are employed to ensure good adhesion between materials. These interesting aspects of MMP make it promising for the fabrication of devices involving different functional layers, such as TENGs.

3D printing has been used for the fabrication of TENGs with tailored properties [37, 38]. Structural modifications and different surface morphology modifications of the triboelectric polymer layer have been carried out using 3D printing to achieve superior structural viability compared to standard micro/nanopatterned moulds [39]. Lately, composite filaments have been studied for 3D-printed TENG applications [40, 41]. These composite filaments have demonstrated improvement in parameters such as triboelectric performance, flexibility, mechanical durability, etc [42–47]. With different varieties of composite filaments now commercially available, fabrication is much easier and more accessible. However, conventional 3D printing is often only capable of printing a single material at a time. This makes it difficult to fabricate devices such as TENGs with different material combinations. Additionally, the multi-step assembly process increases fabrication time and can lead to alignment issues, reducing device efficiency. More importantly, while assembling manually, bonding between different layers can be weak, resulting in mechanical failure, reduced durability, and degraded performance under repeated mechanical stress. These problems can be solved by using MMP, which allows the simultaneous deposition of multiple materials. The stronger bonding between layers allows materials to be deposited together and adhere at the molecular level, improving the mechanical robustness and durability of the device. Furthermore, the capability to print entire device components together can eliminate the need for additional assembly, reduce fabrication time, minimise alignment issues, and enhance precision.

Herein, we introduce an innovative tabletop fabrication method of TENG using MMP. Our design integrates triboelectric layers, current collectors, and substrates using a single-step printing process with commercially available filaments such as nylon 6, acrylonitrile styrene acrylate (ASA), C/PVDF, and C/PLA. Nylon 6 is used as positive triboelectric material because of its electron-donating capability, while ASA and C/PVDF are used as negative triboelectric material considering the electron-accepting properties of ASA and PVDF. C/PLA is used as the current collector, and wood/PLA filament is used as the supporting substrate. The wood/PLA composite is used as the supporting substrate to mimic the texture of the wooden floor and enhance the practicality of the MMP-TENG for floor-based energy generation. To demonstrate the feasibility of this approach, we integrated MMP-TENG with the electronics, and a smart footstep monitoring system was developed. In a nutshell, this work represents a significant advancement in scalable fabrication methods for triboelectric devices, offering a pathway toward cost-effective energy solutions.

2. Results and discussion

The fabrication steps of multi-material 3D-printing of TENG as a smart floor tile are illustrated in Figure 1. A single-stretch fabrication method was employed for the top and bottom layers of TENG consisting of triboelectric materials, conducting current collector and supporting substrate. The top layer was fabricated employing MMP of nylon 6, C/PLA and wood/PLA filaments and the bottom layer was fabricated employing MMP of C/PVDF, C/PLA and wood/PLA. Additionally,

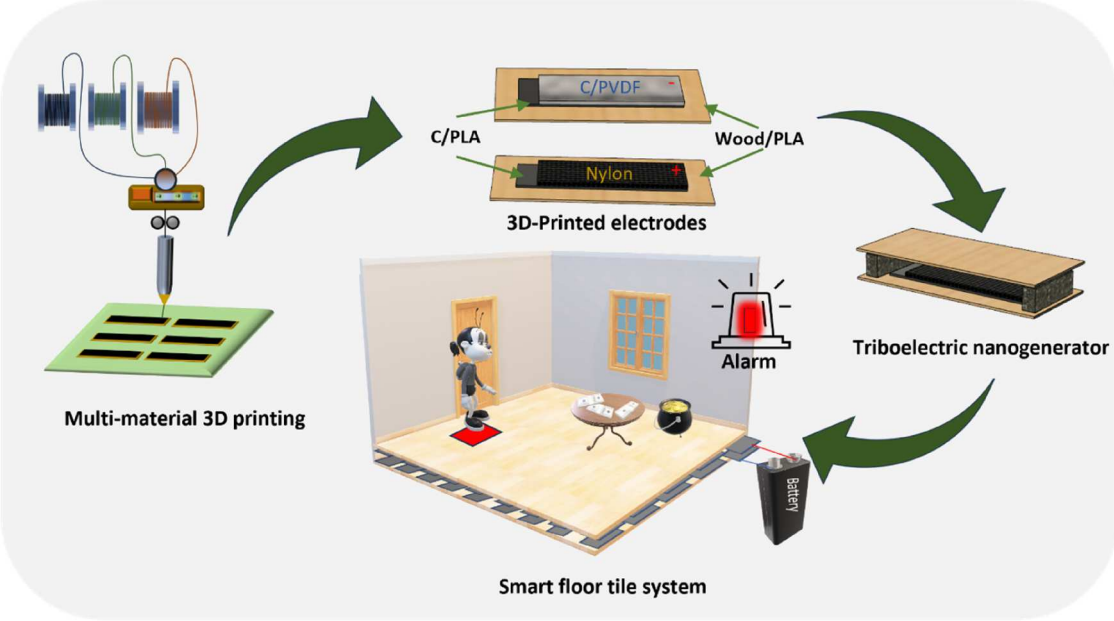

Figure 1. Schematic illustration of multi-material 3D printing of triboelectric nanogenerator and application as smart floor tile.

another bottom layer was fabricated employing MMP of ASA, C/PLA and wood/PLA filaments.

The surface morphology of the positive and negative triboelectric materials were characterised using a confocal laser scanning microscope (CLSM) using a 100x lens, as shown in Figure 2. As all three electrodes were 3D printed, the surface was entirely covered with polymer, with a wave-like pattern on the surface. The 3D-printed surface of the ASA, C/PVDF and nylon 6 are wavy that happened following the top layer printhead movement in a monotonic pattern to fill the 3D structure.

As the surface roughness of the electrodes highly contributes to the output performance of TENG, the CLSM was used to analyse the surface roughness of the electrodes. Figure 3a,d, and g depict the magnified optical images of the ASA, C/PVDF and nylon 6, respectively. The 2D false colour image maps of the topography of ASA, C/PVDF and nylon 6 can be observed in Figure 3b, e, and h, while their corresponding 3D false colour image maps are shown in Figure 3c,f, and i, respectively. The roughness of the electrode surface is clearly visible in the 2D and 3D false-colour images. Furthermore, the average surface roughness value is measured from the CLSM system, which is obtained as 6.36, 11.64, and 22.86 µm for ASA, C/PVDF and nylon 6, respectively. As evident from the optical images, nylon 6 exhibited the highest surface roughness among the tested electrodes. Among negative triboelectrodes, C/PVDF demonstrated a higher surface roughness. This increased roughness can facilitate greater contact area at the microscopic level and enhance the charge transfer and overall triboelectric performance of the TENG.

Compression, tensile, and adhesion tests were carried out to understand the mechanical properties of the 3D-printed TENG on samples: nylon 6-C/PLA, ASA-C/PLA, and C/PVDF-C/PLA. From the compression test, C/PVDF-C/PLA and ASA-C/PLA exhibited good compressive strength of 41.8 and 42.8 MPa, while the nylon 6-C/PLA sample demonstrated a more gradual deformation and compressive strength of 36.1 MPa. Similarly, ASA-C/PLA exhibited a superior tensile strength of 1769 MPa. The tensile strength of C/PVDF-C/PLA was found to be 736.7 MPa. Interestingly, nylon 6-C/PLA exhibited significant ductility with an elongation at the break with a tensile strength of 1169.5 MPa.

The adhesion test was carried out to understand interaction behaviours while printed together. Among the three samples, nylon 6-C/PLA demonstrated the highest adhesion performance with an adhesion strength of 527.1 MPa. This can be due to mechanical interlocking or surface roughness, which contributes to better adhesion with C/PLA. ASA-C/PLA sample also displayed good adhesion at 518.8 MPa, which can be attributed to its molecular composition and high degree of molecular polarity. This allows good bonding and mechanical interlocking with the C/PLA polymer matrix. C/PVDF demonstrated an adhesion strength of 345.4 MPa, showing reasonable bonding due to its fluoropolymer backbone. This fluoropolymer backbone provides good chemical resistance along with moderate adhesion. Interestingly, all three samples fracture at the neck of the sample rather than at the interface. This suggests that the adhesion strength between the materials and C/PLA exceeds the intrinsic tensile strength of the material.

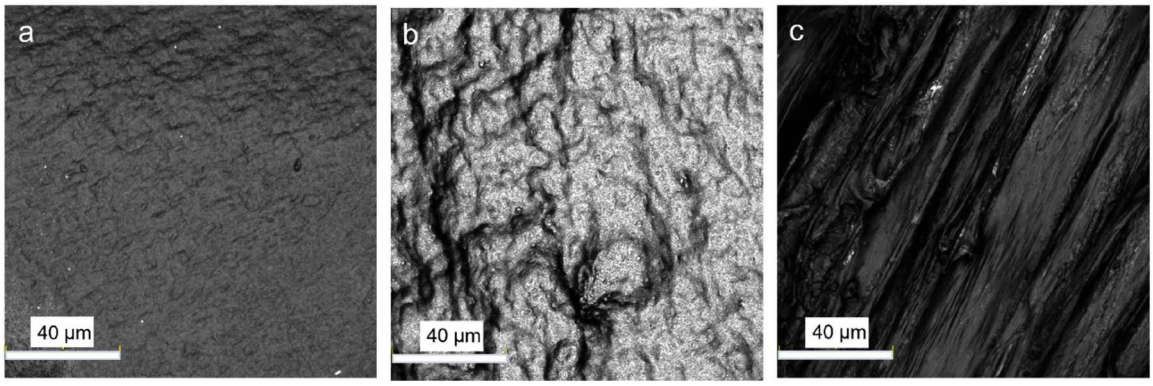

Figure 2. Confocal laser scanning microscopy (CLSM) images at high-magnification of a) ASA, b) C/PVDF and c) nylon 6, respectively.

To provide a better understanding of the operational mechanism of the TENG, a schematic illustration of the working mechanism is shown in Figure 4. Initially, an external force is applied, and both electrodes (triboelectric A and triboelectric B) come into contact with each other. This causes a charge to build up at the interface, as shown in Figure 4b. When the force is released, the separation between the layers establishes a potential difference between the electrodes (Figure 4c). The potential difference induces an electron flow in the

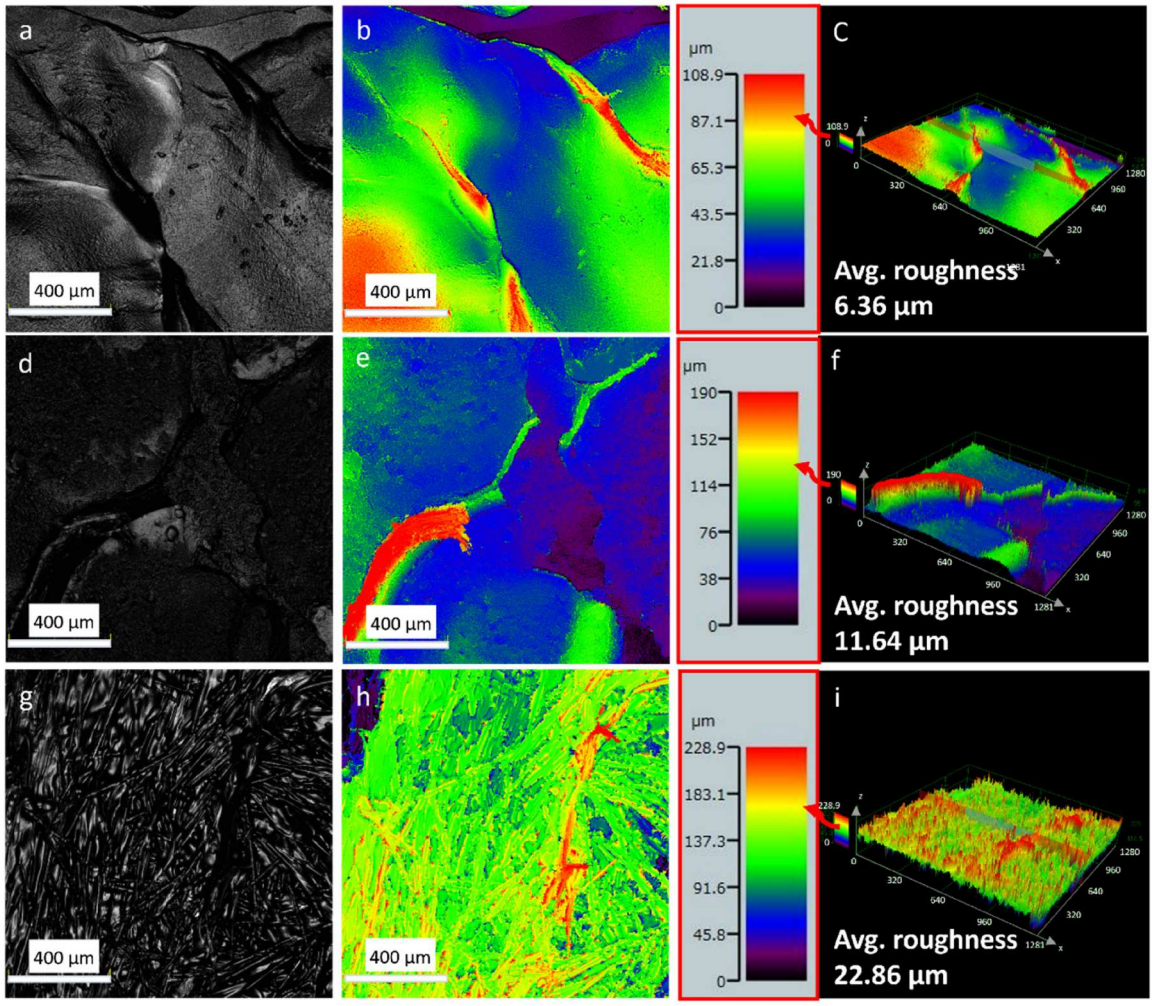

Figure 3. Confocal laser scanning microscope (CLSM) images: a,d,g) at high-magnification, b,e,h) 2D false colour-mapped images, and c,f,i) 3D false colour-mapped images for the topography of ASA, C/PVDF and nylon 6, respectively.

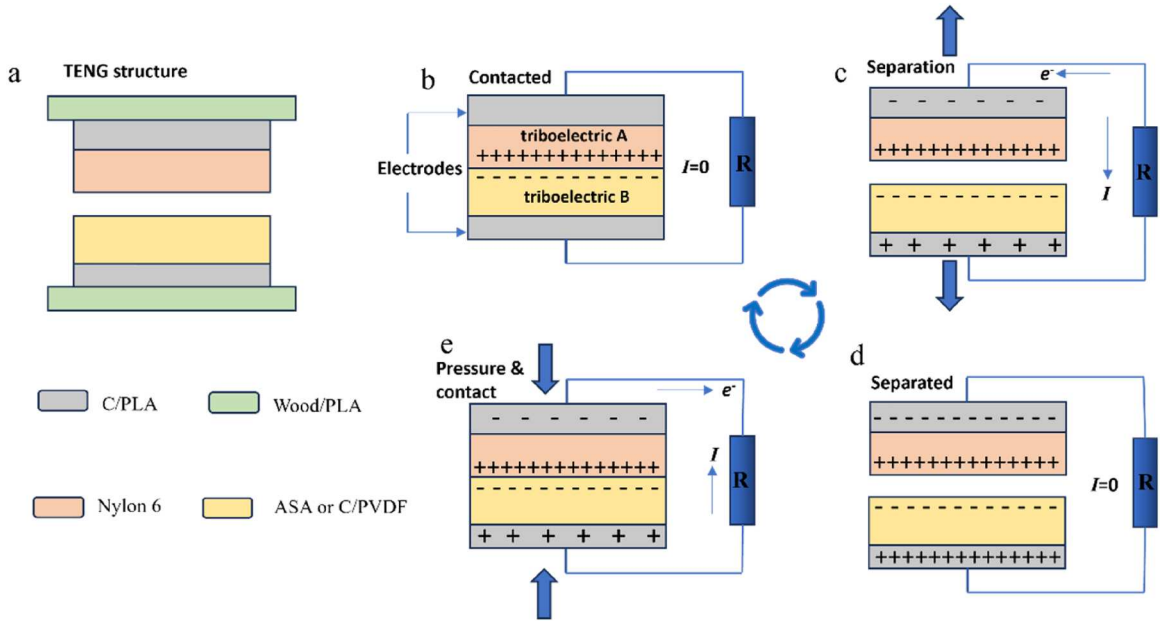

Figure 4. (a) schematic illustration of TENG structure; TENG operating mechanism (a) electrodes in the contacted state. (b) electrodes in a separating state. (c) electrodes in a fully separated state, and (d) electrodes cone again in contact.

external circuit, generating a current. The flow of charges continues until an equilibrium is reached on the surface charges of the electrodes (Figure 4d). While the electrodes are pressed again, the accumulated charges on the electrodes tend to flow in opposite directions, resulting in a reverse flow of current (Figure 4e). Thus, alternating current flow is produced during each pressing and releasing motion.

The triboelectric output performance of the ASA and C/PVDF tribonegative materials against tribopositive nylon 6 are shown in Figure 5. The effect of contact frequency was also determined by systematically increasing oscillation frequency from 8 to 12 Hz at a contact force of 2.8 N, as shown in Figure 5c-f. It was observed that with increasing frequency, the output voltage ($V_{(1x\ probe)}$) and output current ($I_{(gain\ 1x\ +\ 100\Omega)}$) of C/PVDF|nylon 6-TENG are increased. The C/PVDF-based TENG displays a slightly higher peak-to-peak voltage $V_{(1x\ probe)}$ than the ASA-based TENG at all measured contact frequencies. This can be attributed to the presence of fluorine atoms in the repeating monomer units of PVDF, which enhances the electronegativity of PVDF and enhances charge separation during the triboelectric process. The electronegativity difference between fluorine and elements present in nylon 6 promotes the transfer of charges, resulting in effective charge separation during the triboelectric process. In addition, the presence of conductive carbon in C/PVDF creates pathways for efficient charge transport within the PVDF matrix. This improves the movement of generated charges during the triboelectric process. Additionally, the surface roughness of C/PVDF was higher than that of ASA, as noted with CLSM. It was observed that the potential differences between the electrodes in the pressing and releasing cycles are not symmetric for all cases. This can be attributed to the occurrence of several effects like contact electrification, electrostatic induction, and charge redistribution between the electrodes that make the different intensities of alternate signals [48]. Consequently, the C/PVDF|nylon 6-TENG generates a power density of 1.97 μW cm^{-2} and an energy density of 0.16 nJ cm^{-2} at 12 Hz. Whereas ASA-based TENG provides a power density of 1.287 μW cm^{-2} and an energy density of 0.11 nJ cm^{-2} at 12 Hz. Whereas ASA-TENG gave a power density of 1.287 μW cm^{-2} and an energy density of 0.11 nJ cm^{-2} at 12 Hz. Additionally, a cyclic stability test was conducted for 10 h (over 360,000 cycles) to observe the long-term stability of the fabricated TENG device (Figure S5). The average peak-to-peak output voltage showed a slight but consistent increase with the number of cycles. This gradual increase in the output voltage can be attributed to the progressive activation of the triboelectric layers through triboelectrification during the initial cycles [49]. The device reached a stable state with consistent output after a few cycles, highlighting its durability and reliable performance under prolonged operation.

From the electrical results that were encouraging, we proceeded to design a smart floor tile. The illustration of the circuit design is shown in Figure 6a. As dissipated, the TENG is connected to the bridge rectifier to convert the alternating current (AC) to direct current (DC). This

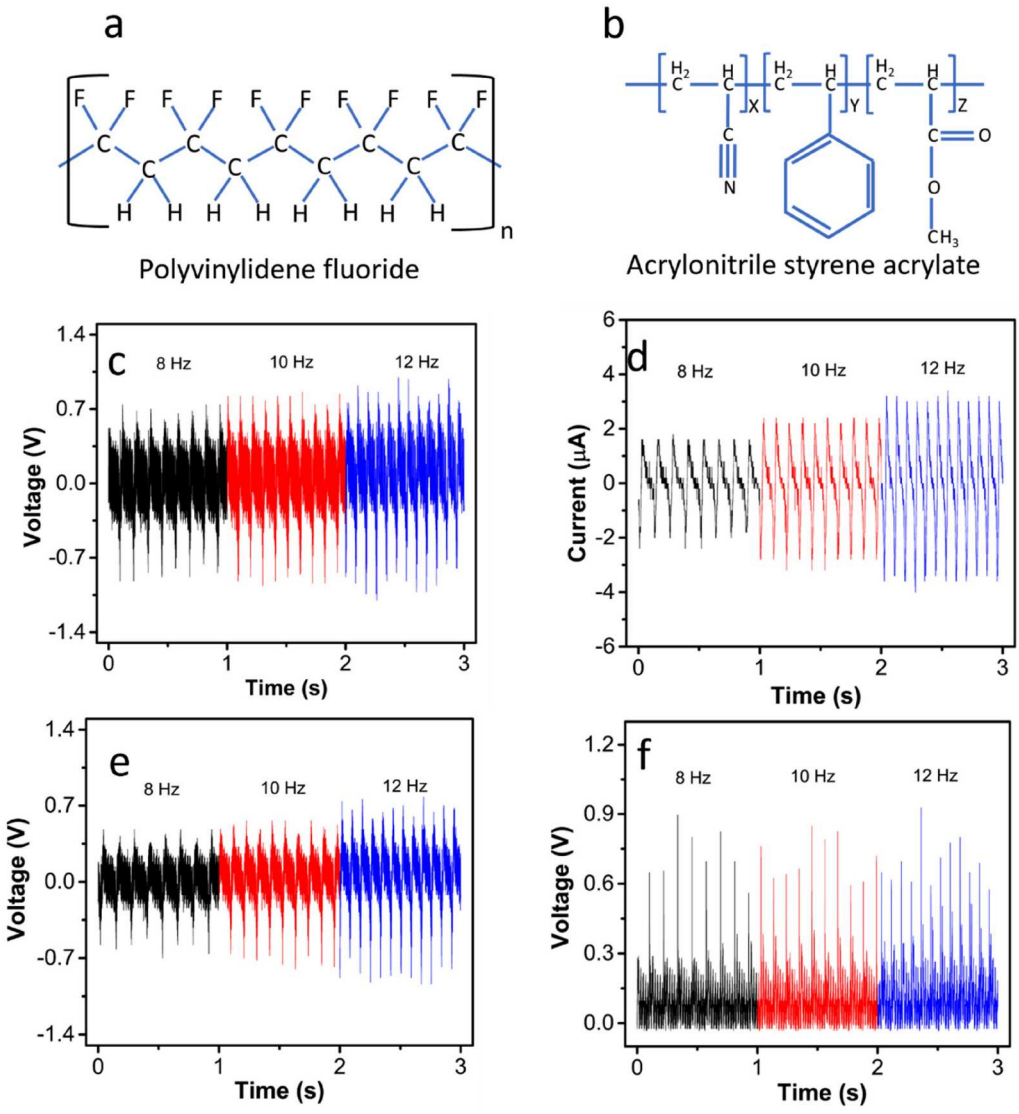

Figure 5. Chemical structure of a) polyvinylidene fluoride (PVDF) b) acrylonitrile styrene acrylate (ASA); Variation of output voltage $V_{(1x\ probe)}$ of (c) C-PVDF and (e) ASA against nylon 6 at different contact frequencies and d) variation of output current ($I_{(gain\ 1x + 100\ \Omega)}$) of C-PVDF|nylon 6 TENG; f) Variation of output voltage at different contact frequencies while connected by a bridge rectifier with the C-PVDF|nylon 6 TENG. Contact force = 2.8 N.

conversion ensures a unidirectional flow of electrical energy that is suitable for further processing. The DC output from the bridge rectifier is then fed to the analog input pin (which can detect fluctuating voltage) of the ATmega2560 microcontroller board, which processes the signal obtained to make a decision based on the programme flashed into it. Here, the ATmega2560 was programmed to give alerts on the LCD display and buzzer. The voltage values below 0.2 V were not considered to avoid noise. This selective attenuation ensures optimal signal-to-noise ratio and enhances the accuracy of data acquisition and processing.

The image in Figure 6b shows multiple TENGs connected in parallel and operating as a switch, showcasing its ability to act as an interface between human interaction and electrical output. This is further quantified in Figure 6c by recording the voltage response from the C/PVDF|nylon 6-TENG with hand-taping. This is further illustrated in Supporting Information Video S2. This illustration not only affirms the functionality of the device as a switch. Such smart switches, along with IoT-enabled devices, can be suitable for applications such as smart doorbells or sensors for touch-sensitive controls. Additionally, the implementation in automotives for touch-sensitive controls will reduce the need for traditional buttons.

Similarly, the image in Figure 6d shows the MMP-TENG's applicability as a miniature form of smart floor tile, which is responsive to foot pressure. Figure 6e shows the voltage output from toe-tapping on the C/

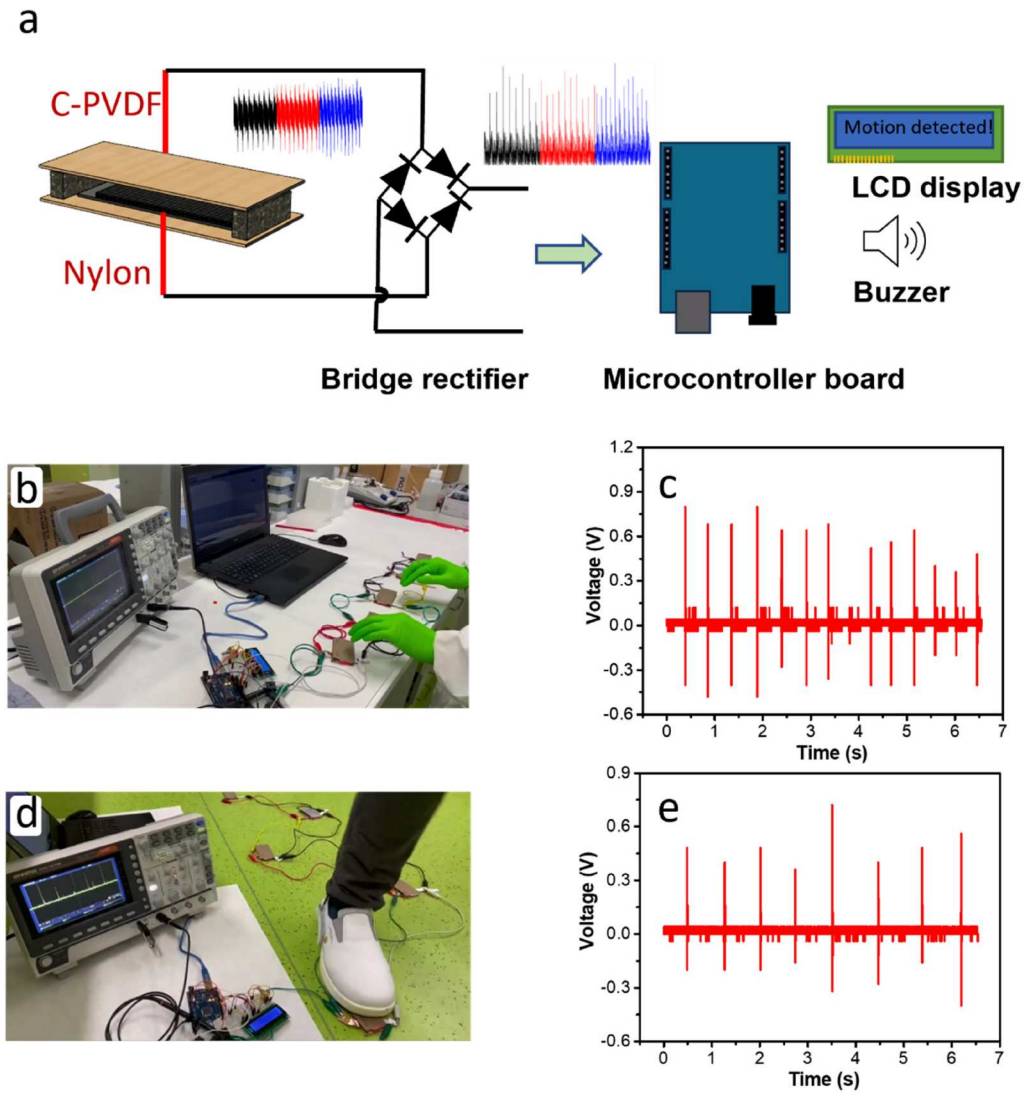

Figure 6. a) Schematic representation of the smart floor tile sensor circuit consisting of C/PVDF|nylon 6-TENG, microcontroller (Arduino mega 2560), I2C 20 × 4 LCD display and a Piezoelectric buzzer, b) optical photograph of TENG operation as a switch, c) voltage output of TENG operation with hand tapping, d) optical photograph of TENG application as smart floor sensor that can be scaled to fabricate a floor tile and e) voltage output of TENG operation with toe-tapping.

PVDF|nylon 6 at periodic intervals. The toe-tapping on MMP-TENG generates an average pk-to-pk output voltage of 600 mV. This shows the possibility of real-time foot-steps or fall detection monitoring. Video S1 (supporting information) presents the real-time footstep monitoring of the MMP-TENG connecting it to a microcontroller circuit. The device cannot only be applied as a footstep monitoring sensor but also can be applied as an energy harvesting device. The MMP-TENG device (foot-print area 2×4 cm^2) generates power of 0.89 µW by simple toe-tapping action, as shown in Video S1. Such MMP TENG sensor can be scaled up to fabricate smart floor tiles that can be integrated into smart buildings to detect occupancy and movements and optimise lighting and climate control. This system can also be useful in public spaces or commercial establishments to monitor foot traffic and enhance banking security systems. In healthcare facilities, this can be used for real-time monitoring of patient movement or patient monitoring systems to provide continuous data on patient activity.

3. Conclusion

Multi-material 3D printing (MMP) based on FDM has been successfully employed for the single-step fabrication of TENG devices, including positive and negative triboelectric layers, current collectors and supporting substrates. Nylon 6 was used as positive triboelectric material, while C/PVDF was employed as negative triboelectric material. A contact-separation mode was employed for the output evaluation of MMP-TENG. The study is expanded by using ASA as a negative triboelectric layer, keeping

nylon 6 as the positive electrode. C/PVDF|nylon 6 – MMP-TENG demonstrated 1.53 times better average power density compared to ASA|nylon 6 – MMP-TENG. A real-time application of C/PVDF|nylon 6 MMP-TENG was demonstrated by integrating with electronics for smart floor tile and a smart switch. This effectively showcases the ability and effectiveness of MMP-TENG to operate as a real-time, self-powered sensor.

This work demonstrates the potential of MMP for the single-step fabrication of TENG. On the other hand, FDM printing is only possible on certain materials due to the intrinsic material properties and thermal requirements of the process. Furthermore, material combinations must be carefully selected to ensure strong interlayer bonding. Additionally, current FDM printing technology cannot achieve nanoscale detail fabrication that could be beneficial for TENG applications. However, it is important to note that the presented device is a prototype and is meant to be used in ambient environmental conditions. As PLA-based substrate and current collector are used, its susceptibility to degradation under humid, acidic, or alkaline conditions limits its applicability in harsh environments [50, 51]. As such, this prototype is best suited for specific applications where environmental influences are negligible, such as fall monitoring systems for elderly people or security monitoring floors in stable indoor conditions.

Moreover, there are several possibilities to explore in this work to tune and optimise triboelectric performance for various applications. This includes examining the broader range of materials that are both triboelectric and compatible with FDM printing. As triboelectric properties are affected by surface roughness, various surface designs can be explored to obtain maximum output. Different surface treatments can affect the charge transfer properties and need to be investigated further. A study on the long-term performance of the device under different environmental conditions will also be beneficial for real-time implementation.

4. Experimental section

Materials/Filaments: C/PVDF 3D printing filaments were obtained from 3dogg.com, Netherlands, while Nylon 6 (GF30-PA6) was obtained from BASF 3D Printing Solutions, Germany. Timberfill® filaments (wood/PLA) were received from Fillamentum Manufacturing Czech s.r.o. in the Czech Republic. Protopasta filaments (C/PLA) were purchased from ProtoPlant in British Columbia. ASA Jet Black filament was procured from Prusa Research a.s., Czech Republic.

Fabrication of multi-materials 3D-printed Triboelectric Nanogenerator device: The TENG electrodes were designed using the open-access software Autodesk Fusion 360. Each layer of TENG was placed as a different component (or body) to allow for distinct material assignments during the printing process. Then, the components are converted to mesh format and exported in *.stl* format. This *.stl* is then imported to the PrusaSlicer software and split into parts. Each individual parts are assigned a particular filament and printing parameters. Then the file is sliced using PrusaSlicer 2.5.0 software to obtain a *.gcode* file for 3D printing. These designs were printed using a multi-material unit (MMU), which is attached to a Prusa 3D printer (Prusa i3 MK3S, Czech Republic). The Prusa slicer design of the TENG electrode design is illustrated in Figure S1. 3D printing was carried out using commercially available filaments: wood/PLA (Timberfill) and C/PLA (Protopasta) acted as the substrate (8 cm × 4 cm × 2 mm), and current collectors (6 cm × 3 cm × 0.3 mm), respectively, for both the positive and negative electrodes (5 cm × 3 cm × 0.3 mm). Nylon 6 was used as the positive triboelectric material, while C/PVDF and ASA were used as the negative triboelectric materials. For the 3D printing, the bed temperature was set to 60 °C, while the nozzle temperatures were set to 215 °C for wood/PLA, 220 °C for C/PLA, 250 °C for nylon 6, 250 °C for C/PVDF, and 260 °C for ASA. Infill was set at 90% for all printing. The printing speed was set using the default PrusaSlicer software settings, which optimise parameters based on the material and printer model. The printing speed was set as follows: perimeters at 45 mm/s, small and external perimeters at 25 mm/s, infill and solid infill at 70 mm/s, and top solid infill at 45 mm/s.

Materials Characterisation: The morphological analysis and optical and height profile images of the surface of triboelectric materials were carried out using CLSM (Olympus Lext OLS4100). The laser of wavelength 405 nm was used for CLSM.

Mechanical characterisation: Mechanical tests were conducted using a universal testing machine, Z010 AllroundLine, by ZwickRoell. The samples were prepared with different multi-material interfaces to evaluate their mechanical performance under compressive forces. A loading rate of 2 mm/min was used to compress the samples. The samples were prepared by printing in a cylindrical shape with both a diameter and height of 6 mm (Figure S2a). The first 3 mm was printed with C/PLA for all samples, and then the other 3 mm was printed with the dielectric material (i.e. C/PVDF, ASA or nylon 6). Similarly, tensile test samples were prepared in dog bone shape (Figure S3a). The sample length of 35 and 2 mm thickness was prepared. For all samples, the first 1 mm printed with C/PLA for all samples and top 1 mm with triboelectric material. The loading rate of 2 mm/min was applied. Adhesion samples were

prepared by sandwiching the different materials (Figure S4a). Each material was 101.6 mm long, with 24.5 mm overlapping with each other. A similar loading rate of 2 mm/min was applied to the samples till breaking.

Electrical measurement: The voltage measurement of the TENG was recorded using a digital oscilloscope (GW Instek GDS-1074B) using a 1x probe. The current measurements were carried out using a custom-made I – V converter that is connected to the oscilloscope. The periodic mechanical perturbations for the measurement were produced using a linear motor actuator with a hub 20 mm (24 V DC, max 1000 rpm, DAOE). 2.8 N constant force was maintained for all measurements. The average power density and energy density were calculated using the formula.

$$P = \frac{\left(\frac{V^2}{R}\right)}{a}$$

$$E = P * t$$

Where P is the power density, V is the average peak-to-peak voltage, R is the resistance, E is the energy density, t is the time for a single cycle, and a is the area of triboelectric material.

Authors contribution

S.M and K.G have contributed equally. S.M. and K.G. carried out fabrication, characterisations, and analysis. S.M. wrote the first draft. K.G. conceptualised and mentored the whole project, and reviewed and edited the manuscript. M.P. supervised the project and provided the research direction. All authors contributed to the writing.

Disclosure statement

No potential conflict of interest was reported by the author(s).

Funding

This work was supported by ERDF/ESF project TECHSCALE (No. CZ.02.01.01/00/22_008/0004587). This research was cofunded by the European Union under the REFRESH—Research Excellence For REgion Sustainability and High-tech Industries project number CZ.10.03.01/00/22_003/0000048 via the Operational Programme Just Transition. CzechNanoLab project LM2023051, funded by MEYS CR, is gratefully acknowledged for the financial support of the measurements/sample fabrication at CEITEC Nano Research Infrastructure.

Data availability statement

The data that support the findings of this study are available from the corresponding author, M.P., upon reasonable request.

References

[1] Javaid M, Haleem A, Rab S, et al. Sensors for daily life: a review. Sens Int. 2021;2:100121.
[2] Jiang S, Cheng R, Wang X, et al. Real-time electrical detection of nitric oxide in biological systems with sub-nanomolar sensitivity. Nat Commun. 2013;4(1):2225.
[3] Jin L, Tao J, Bao R, et al. Self-powered real-time movement monitoring sensor using triboelectric nanogenerator technology. Sci Rep. 2017;7(1):10521.
[4] Ates HC, Nguyen PQ, Gonzalez-Macia L, et al. End-to-end design of wearable sensors. Nat Rev Mater. 2022;7(11):887–907.
[5] Kumar A. Recent progress in the fabrication and applications of flexible capacitive and resistive pressure sensors. Sens Actuators A: Phys. 2022;344:113770.
[6] Pu J, Ma K, Luo Y, et al. Textile electronics for wearable applications. Int J Extreme Manuf. 2023;5:042007.
[7] Xu Z, Cao LNY, Wang ZL. Triboelectric nanogenerators for scientific instruments and devices. Adv Devices Instrum. 2024;5:0026.
[8] Li Q, Fu S, Yang H, et al. Achieving ultrahigh DC-power triboelectric nanogenerators by lightning rod-inspired field emission modeling. Research. 2024;7:0437.
[9] Jan AA, Kim S, Kim S. A skin-wearable and self-powered laminated pressure sensor based on triboelectric nanogenerator for monitoring human motion. Soft Sci. 2024;4:10.
[10] Luo L, Liu C, Gu R, et al. Constructing high-performance and versatile liquid–solid triboelectric nanogenerator with inflatable columnar units. Int J Extreme Manuf. 2025;7(1):015505.
[11] Li Z, Yang C, Zhang Q, et al. Standardized volume power density boost in frequency-up converted contact-separation mode triboelectric nanogenerators. Research. 2023;6:0237.
[12] Lee D, Chae J, Cho S, et al. Bidirectional rotating direct-current triboelectric nanogenerator with self-adaptive mechanical switching for harvesting reciprocating motion. Int J Extreme Manuf. 2024;6(4):045502.
[13] Fan FR, Tian ZQ, Lin Wang Z. Flexible triboelectric generator. Nano Energy. 2012;1(2):328–334.
[14] Cheng T, Shao J, Wang ZL. Triboelectric nanogenerators. Nat Rev Methods Primers. 2023;3(1):39.
[15] Khandelwal G, Maria Joseph Raj NP, Kim SJ. Materials beyond conventional triboelectric series for fabrication and applications of triboelectric nanogenerators. Adv Energy Mater. 2021;11(33):2101170.
[16] Zou H, Zhang Y, Guo L, et al. Quantifying the triboelectric series. Nat Commun. 2019;10(1):1427.
[17] Mahmud MAP, Lee JJ, Kim GH, et al. Improving the surface charge density of a contact-separation-based triboelectric nanogenerator by modifying the surface morphology. Microelectron Eng. 2016;159:102–107.
[18] Dharmasena RDIG, Silva SR. Towards optimized triboelectric nanogenerators. Nano Energy. 2019;62:530–549.
[19] Dharmasena RDIG, Deane JHB, Silva SR. Nature of power generation and output optimization criteria for triboelectric nanogenerators. Adv Energy Mater. 2018;8(31):1802190.
[20] Zhang H, Quan L, Chen J, et al. A general optimization approach for contact-separation triboelectric nanogenerator. Nano Energy. 2019;56:700–707.

[21] Shao J, Yang Y, Yang O, et al. Designing rules and optimization of triboelectric nanogenerator arrays. Adv Energy Mater. 2021;11(16):2100065.
[22] Ali MA, Hu C, Yttri EA, et al. Recent advances in 3D printing of biomedical sensing devices. Adv Functional Mater. 2022;32(9):2107671.
[23] Fan J, Bai J, Ma H, et al. All-3D-printed multifunctional wearable energy systems with embodied zinc-ion storage capability and smart responsive effect. Energy Storage Mater. 2023;55:12–20.
[24] Zhu Z, Ng DWH, Park HS, et al. 3D-Printed multifunctional materials enabled by artificial-intelligence-assisted fabrication technologies. Nat Rev Mater. 2021;6(1):27–47.
[25] Cano-Vicent A, Tambuwala MM, Hassan SS, et al. Fused deposition modelling: current status, methodology, applications and future prospects. Addit Manuf. 2021;47:102378.
[26] Cai N, Sun P, Jiang S. Rapid prototyping and customizable multifunctional structures: 3D-printing technology promotes the rapid development of TENGs. J Mater Chem A. 2021;9(30):16255–16280.
[27] Mappoli S, Ghosh K, Pumera M. MXene and polyaniline coated 3D-printed carbon electrode for asymmetric supercapacitor. Virtual Phys. Prototyp. 2024;19(1):e2361139.
[28] Han D, Lee H. Recent advances in multi-material additive manufacturing: methods and applications. Curr Opin Chem Eng. 2020;28:158–166.
[29] Yin J, Lu C, Fu J, et al. Interfacial bonding during multi-material fused deposition modeling (FDM) process due to inter-molecular diffusion. Mater Des. 2018;150:104–112.
[30] Singh R, Kumar R, Farina I, et al. Multi-material additive manufacturing of sustainable innovative materials and structures. Polymers (Basel). 2019;11(1):62.
[31] Li Y, Wu Z, Chen Y, et al. Multi-material embedded 3D printing for one-step manufacturing of multifunctional components in soft robotics. Addit Manuf. 2024;85:104178.
[32] Rafiee M, Farahani RD, Therriault D. Multi-material 3D and 4D printing: a survey. Adv Sci. 2020;7(12):1902307.
[33] Goh GL, Goh GD, Nguyen VP, et al. A 3D printing-enabled artificially innervated smart soft gripper with variable joint stiffness. Adv Mater Technol. 2023;8(24):2301426.
[34] Emon MOF, Alkadi F, Philip DG, et al. Multi-material 3D printing of a soft pressure sensor. Addit Manuf. 2019;28:629–638.
[35] Ruiz OG, Dhaher Y. Multi-color and multi-material 3D printing of knee joint models. 3D Print Med. 2021;7(1):12.
[36] Alarifi IM. Revolutionising fabrication advances and applications of 3D printing with composite materials: a review. Virtual Phys. Prototyp. 2024;19(1):e2390504.
[37] Chen B, Tang W, Jiang T, et al. Three-dimensional ultraflexible triboelectric nanogenerator made by 3D printing. Nano Energy. 2018;45:380–389.
[38] Wang J, Wu B, Liu G, et al. Flexure hinges based triboelectric nanogenerator by 3D printing. Extreme Mech Lett. 2018;20:38–45.
[39] Mahmud MAP, Zolfagharian A, Gharaie S, et al. 3D-printed triboelectric nanogenerators: state of the art, applications, and challenges. Adv Energ Sust Res. 2021;2(3):2000045.
[40] Akin S, Chang T, Abir SSH, et al. One-step fabrication of functionalized electrodes on 3D-printed polymers for triboelectric nanogenerators. Nano Energy. 2024;129:110082.
[41] Zheng R, Chen Y, Chi H, et al. 3D printing of a polydimethylsiloxane/polytetrafluoroethylene composite elastomer and its application in a triboelectric nanogenerator. ACS Appl Mater Interfaces. 2020;12(51):57441–57449.
[42] Ghosh K, Pumera M. MXene and MoS3−x Coated 3D-printed hybrid electrode for solid-state asymmetric supercapacitor. Small Methods. 2021;5(8):2100451.
[43] Browne MP, Redondo E, Pumera M. 3D printing for electrochemical energy applications. Chem Rev. 2020;120(5):2783–2810.
[44] Redondo E, Muñoz J, Pumera M. Green activation using reducing agents of carbon-based 3D printed electrodes: turning good electrodes to great. Carbon N Y. 2021;175:413–419.
[45] Perales-Rondon JV, Rojas D, Gao W, et al. Copper 3D-printed electrodes for ammonia electrosynthesis via nitrate reduction. ACS Sustain Chem Eng. 2023;11(18):6923–6931.
[46] Fojta M, Hermanová M, Pivoňková H, et al. Genosensing on a 3D-printed nanocarbon electrode. Electrochem Commun. 2023;151:107508.
[47] Goh GL, Lee S, Cheng SH, et al. Enhancing interlaminar adhesion in multi-material 3D printing: a study of conductive PLA and TPU interfaces through fused filament fabrication. Mater Sci Addit Manuf. 2024;3(1):2672.
[48] Ghosh K, Iffelsberger C, Konečný M, et al. Nanoarchitectonics of triboelectric nanogenerator for conversion of abundant mechanical energy to green hydrogen. Adv Energy Mater. 2023;13(11):2203476.
[49] Ghosh K, Morgan A, Garcia-Casas X, et al. Tailoring of self-healable polydimethylsiloxane films for mechanical energy harvesting. ACS Appl Energy Mater. 2024;7(19):8185–8195.
[50] Zaaba NF, Jaafar M. A Review on degradation mechanisms of polylactic acid: hydrolytic, photodegradative, microbial, and enzymatic degradation. Polym Eng Sci. 2020;60(9):2061–2075.
[51] Elsawy MA, Kim KH, Park JW, et al. Hydrolytic degradation of polylactic acid (PLA) and its composites. Renewable Sustainable Energy Rev. 2017;79:1346–1352.